Remote Sensing of Environment 324 (2025) 114763

Contents lists available at ScienceDirect

Remote Sensing of Environment

journal homepage: www.elsevier.com/locate/rse

# Slip surface, volume and evolution of active landslide groups in Gongjue County, eastern Tibetan Plateau from 15-year InSAR observations

Bo Chen [a,b,c,f], Zhenhong Li [a,b,d,*], Chuang Song [a,b,d,*], Chen Yu [a,b,d], Roberto Tomás [f], Jiantao Du [a,b,c,f], Xinlong Li [a,b,c], Adrien Mugabushaka [a,b,c], Wu Zhu [a,b,e], Jianbing Peng [a,b,d]

[a] College of Geological Engineering and Geomatics, Chang'an University, Xi'an 710054, China
[b] State Key Laboratory of Loess Science, Xi'an 710054, China
[c] Big Data Center for Geosciences and Satellites, Xi'an 710054, China
[d] Key Laboratory of Western China's Mineral Resources and Geological Engineering, Ministry of Education, Xi'an 710054, China
[e] Key Laboratory of Ecological Geology and Disaster Prevention, Ministry of Natural Resources, Xi'an 710054, China
[f] Department of Civil Engineering, University of Alicante, Alicante 03080, Spain

ARTICLE INFO

Edited by Jing M. Chen

*Keywords:*
InSAR
Slip surface
Landslide volume
Slide type
Landslide dynamics

ABSTRACT

Landslides stand as a prevalent geological risk in mountainous areas, presenting substantial danger to human habitation. The slip surface (SSF), volume, type and evolution of landslides constitute crucial information from which to understand landslide mechanisms and assess landslide risk. However, current methods for obtaining this information, relying primarily on field surveys, are usually time-consuming, labor-intensive and costly, and are more applicable to individual landslides than large-scale landslide groups. To tackle these challenges, we present a novel method utilizing multi-orbit Synthetic Aperture Radar (SAR) data to deduce the SSF, volume and type of active landslides. In this method, the SSF of landslides over a wide area is determined from three-dimensional deformation fields by assuming that the most authentic direction of the landslide movement aligns parallel to the SSF, on the basis of which the volume and type of active landslides can also be inferred. This approach was utilized with landslide groups in Gongjue County (LGGC), situated in the eastern Tibetan Plateau, which pose grave peril to community members and critical construction along the upstream/downstream of the Jinsha River. Firstly, SAR images were gathered and interferometrically processed from four separate platforms, spanning the period from July 2007 to August 2022. Then, three-dimensional displacement time series were inverted based on Interferometric Synthetic Aperture Radar (InSAR) observations and a topography-constrained model, from which the SSF, volume and type were determined using our proposed method. Finally, the Tikhonov regularization method was applied to reconstruct 15-year displacement time series along the sliding surface, and potential driving factors of landslide motion were identified. Results indicate that 53 landslides were detected in the LGGC region, of which ~70 % were active and complex landslides with maximum cumulative displacement along the sliding surface reaching 1.5 m over the past ~15 years. In addition, the deepest SSF of these landslides was found to reach 114 m, with volumes ranging from $1.66 \times 10^5$ $m^3$ to $1.72 \times 10^8$ $m^3$. Independent in-situ measurements validate the reliability of the SSF obtained in this study. More particularly, we found that the 2018 failure of the Baige landslide (approximately 50 km from LGCC) had caused persistent acceleration to those wading landslides, highlighting the prolonged impact of external factors on landslide evolution. These insights provide a deeper understanding of landslide dynamics and mechanisms, which is crucial when implementing early warning systems and forecasting future failure events.

## 1. Introduction

Landslides rank among the most destructive geohazards globally, widely distributed in mountainous regions, river valleys and coastal areas (Guzzetti et al., 2012; Hungr et al., 2013; Li et al., 2023). They pose serious threats to human lives and property. Landslides initiate

* Corresponding authors at: College of Geological Engineering and Geomatics, Chang'an University, Xi'an 710054, China.
*E-mail addresses:* zhenhong.li@chd.edu.cn (Z. Li), chuang.song@chd.edu.cn (C. Song).

https://doi.org/10.1016/j.rse.2025.114763
Received 19 November 2024; Received in revised form 7 April 2025; Accepted 11 April 2025
Available online 16 April 2025
0034-4257/

when soil or rock masses detach along a weak structural interface, termed the slip surface (SSF) (Jaboyedoff et al., 2020). The SSF determines the size of landslide movement and is a critical research target for landslide prevention and mitigation (Baum et al., 1998; Jaboyedoff et al., 2020; Kang et al., 2023). Accurate identification of the depth and geometric characteristics of the SSF is essential for understanding landslide mechanisms, assessing landslide risks and designing mitigation measures (Carter and Bentley, 1985a; Intrieri et al., 2020). Therefore, SSF research continues to be a crucial topic in landslide hazards.

Current methodologies for identifying SSF are categorized into contact and non-contact. Contact methods include borehole, deep displacement detection, electrical resistivity tomography (ERT) and ground-based radar technology (Intrieri et al., 2020). These approaches, while accurate require a significant investment of time and labor, making them impractical for estimating the volume of landslide groups over a wide area. Non-contact methods are mainly divided into four categories: i) Empirical formula method, employed to determine the relationship between the surface area and volume of landslide, which has relatively low accuracy (Jaboyedoff et al., 2020); ii) Model estimation methods (e.g., the balanced cross section methods (Aryal et al., 2015), elastic dislocation model (Saroli et al., 2021), non-Newtonian viscous flow model (Handwerger et al., 2015) and mass conservation method (Hu et al., 2018), which involve assumptions inherent in the models and have limited applicability; iii) Failure surface estimation method based on morphology (Jaboyedoff et al., 2020), which requires professional geological experts to identify the scarp of the landslide and has a low level of automation, making it challenging to achieve large-scale landslide volume estimation (Jaboyedoff et al., 2020); and iv) Volume estimation method based on surface displacements. Assuming that the direction of movement of the landslide is parallel to the SSF, several studies have utilized two-dimensional displacements (*E*-W and vertical) derived from InSAR to draw a geometric estimation of the SSF along profiles using vector inclination methods (e.g., Crippa et al., 2021; Intrieri et al., 2020). However, this latter method has two shortcomings: 1) It can only obtain the geometry of the SSF along a profile; and 2) Two-dimensional displacements cannot reflect the true movement of the landslide and thus fail to accurately determine the SSF. Therefore, there remains a lack of semi-automated methods based on quasi-3D displacement fields to estimate the SSF and volume of active landslides on a large scale. In this study, we proposed a method for determining the SSF of large-scale landslides using multi-orbit SAR imagery, based on the assumption that ground surface displacement vectors are parallel to the landslide SSF, and validated it in the Jinsha River basin on the Qinghai-Tibet Plateau.

The distinctive topography and geomorphology of the Qinghai-Tibet Plateau contribute to a variety of conditions that are conducive to landslide disasters, especially in the Jinsha River basin. As a result, this region has experienced significant landslide events, including the Baige landslide, the Temi paleo-landslide and the Woda paleo-landslide (Fan et al., 2019; Li et al., 2021; Zhang et al., 2022). This study focuses on the landslide group in Gongjue County (LGGC), located along the Jinsha River 50 km downstream of the Baige landslide. The LGGC spans four towns (Luomai, Shandong, Mindu and Xiongsong), encompassing 27 villages with a resident population of 9470 (https://www.stats.gov.cn/sj/pcsj). The persistent activity of the LGGC poses a threat to the upstream construction of the transportation corridor (Wang et al., 2023), 7 upstream hydropower stations and 20 downstream stations. Determining the SSF, volume, type and long-term displacement of landslides is fundamental to understanding the mechanism and risk of landslides. However, to date, international scholars have predominantly focused their research on individual landslides (Li et al., 2021; Liu et al., 2021; Yao et al., 2022; Zhu et al., 2024) or the location of landslide groups (Zhang et al., 2022; Li et al., 2023) in the LGGC area. The SSF, volume, type and long-term displacement along the sliding surface of landslides within LGGC have yet to be investigated.

This study has mainly focused on conducting a comprehensive investigation of LGGC, employing an integrated observation strategy that combines space-borne radar/optical remote sensing, airborne optical imagery and field campaigns. In particular, we have addressed the challenge of estimating the volume of a large-scale landslide group and long-term deformation along the sliding surface. In the study, we first used three-orbit SAR data, composing C- and L-bands to derive three LOS displacement velocities. An inventory of LGGC was compiled by integrating multi-temporal satellite optical remote sensing images. Subsequently, based on a topography-constrained model and the LOS displacements velocity from three orbits, the quasi-3D displacements field of LGGC was mapped. Furthermore, the study calculated the landslide slip surface slope (LSSS), classified slide types by the LSSS and estimated their volumes. Finally, the study explored the evolutionary mechanisms and triggering factors of LGGC by analyzing 15-year deformation history.

## 2. Study area and data

### *2.1. Gongjue County landslide group*

The study area is located upstream of the Jinsha River valley, on the southeast edge of the Qinghai-Tibet Plateau, at the intersection of Gongjue County in Tibet and Baiyu County in Sichuan, China, within the active tectonic zone of the Jinsha River. It spans an approximate area of 850 $km^2$ (Fig. 1).

The Jinsha River basin constitutes China's foremost hydroelectric hub, contributing over 40 % of the Yangtze River's total hydroelectric potential (Xiao et al., 2022). This region exhibits intricate topography, geomorphology and geological structures, characterized by steep mountain gorges, sharp longitudinal river slopes and fragmented rock formations. Consequently, the area is susceptible to the widespread occurrence of massive landslides. Elevation ranges from 2600 to 4900 m above sea level, with the "V" shaped valleys being the predominant feature in the study area. The terrain features slopes ranging from 10° to 50°. Notably, monthly temperature fluctuations are significant (Wang et al., 2023). Annual rainfall averages 480 mm, approximately 90 % of which occurs between April and September. The study area intersects with several major active fault zones, including the Jinsha River Fault and the Batang Fault, displaying a record of frequent seismic activity. USGS records highlight 16 earthquakes of a magnitude greater than Mw 5.0 within the study area (29–32° N; 98–101° W) between 1900 and

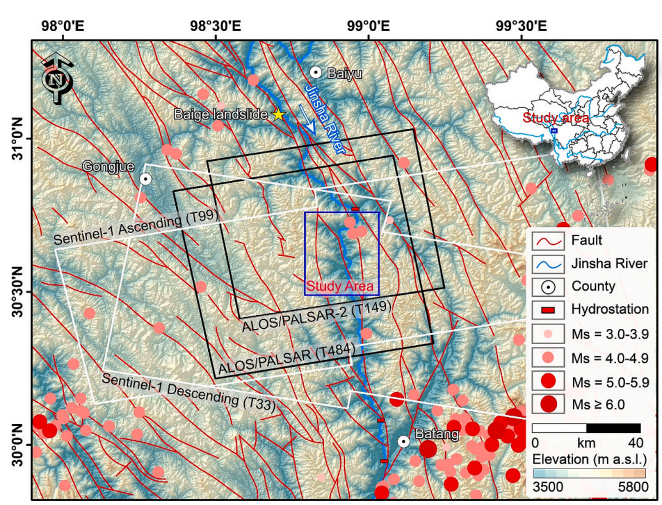


**Fig. 1.** Regional tectonic setting of study area. White and black rectangles show coverage of SAR images. Blue rectangle shows LGGC and red lines are faults – from GeoCloud (https://geocloud.cgs.gov.cn/). Red dots denote earthquakes occurring within study area from 1908 to 2022 – from USGS. Base map is the 1 arc-second DEM from the SRTM. (For interpretation of the references to colour in this figure legend, the reader is referred to the web version of this article.)

2022. Predominant rock types within the landslide groups consist mainly of relatively hard slate and quartz sandstone and soft and hard alternating phyllite (Fig. 2b). The land cover is predominantly grassland (Fig. 2c).

### 2.2. Datasets

We conducted an extensive analysis by integrating and analyzing a vast dataset spanning approximately 15 years (Fig. 3). The dataset included diverse remote sensing datasets, such as satellite SAR images, satellite optical images and regional airborne ortho-photographs. Additionally, we integrated publicly available datasets on rainfall and land surface temperature, as well as information on land cover, lithology and field geomorphological surveys.

The satellite SAR dataset included 391 images, comprising ascending ALOS/PALSAR images from July 2007 to August 2010, ascending ALOS/PALSAR-2 images from February 2016 to May 2020, and ascending and descending Sentinel-1 images from October 2014 to August 2022 (Table 1). These datasets were primarily used to invert quasi-3D displacement fields of LGGC and analyze the 15-year temporal evolution of landslide movements.

Satellite optical remote sensing mainly included Sentinel-2 images from January 2017 to August 2022 and historical Google Earth archive images. These data were primarily used to interpret landslides and analyze changes in the geomorphological features of landslides.

To gain a more detailed understanding of active landslides, we conducted a survey using unmanned aerial vehicle (UAV) and employed structure-from-motion/Multiview stereo photogrammetry to map two landslides (Nos. 25 and 26) and their surroundings on 12 July 2021 and 23 October 2023. We used the FEIMA E2000 flying platform at an altitude of 1000 m above ground surface (Fig. S1). The heading and lateral overlap during flight were 80 % and 70 %, respectively, resulting in a total of 436 RGB images. We generated a Digital Surface Model (DSM) and Digital Ortho-photo Model (DOM) with a resolution of around 17 cm/pixel using Agisoft PhotoScan software (https://www.agisoft.com). The DSM was used to evaluate the impact of Shuttle Radar Topography Mission (SRTM) DEM alignment on quasi-3D displacement results and landslide volume estimation, and the DOM was applied to analyze geomorphological features of the landslides. Additionally, field investigations were conducted in LGGC, and photos taken by UAV and camera were obtained (Fig. 2d-k). These photographs were primarily used to validate the reliability of the landslide detection results.

We collected rainfall datasets from July 2007 to January 2023 from the Climate Hazards Group Infra-Red Precipitation with Station dataset (CHIRPS) (Funk et al., 2015) on the Google Earth Engine (GEE) platform. Land surface temperature (LST) datasets were collected from the GEE platform's MOD11A1 V6.1 product, which provides daily LST in a 1200 $\times$ 1200 km grid. Long-term rainfall and LST data were primarily used to investigate the relationship between landslide movement and these environmental factors. Land cover data for 2020, with resolution of 30 m, were derived from the Chinese Academy of Sciences (Zhang et al., 2021). Lithology data were obtained from GeoCloud. The SRTM DEM was utilized to estimate the quasi-3D displacement of landslides inversely and to mitigate the topographic effects in the InSAR process.

## 3. Methodology

This section introduces a novel strategy that integrates long-term

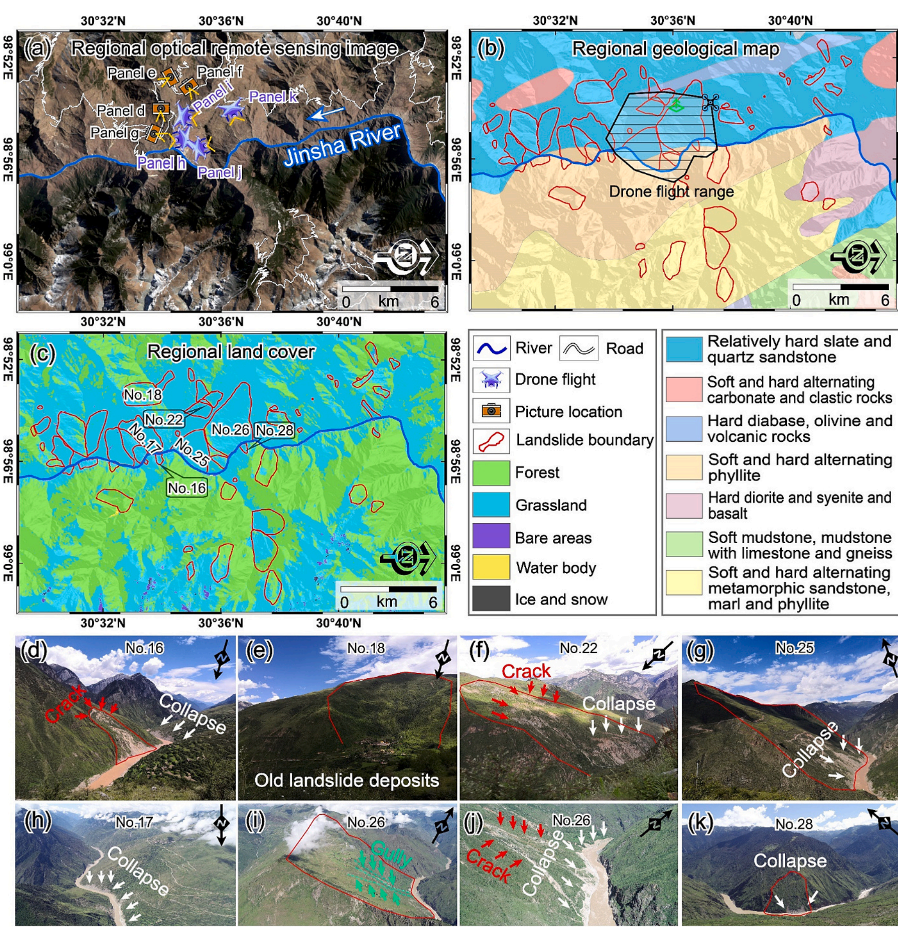


**Fig. 2.** (a) Regional optical remote sensing. (b) Regional geological map. (c) Regional land cover. (d) to (g) Photographs captured in field of landslide Nos. 16, 18, 22 and 25, respectively. (h) to (k) Pictures of the UAV survey performed on landslide Nos. 17, 26 and 28, respectively.

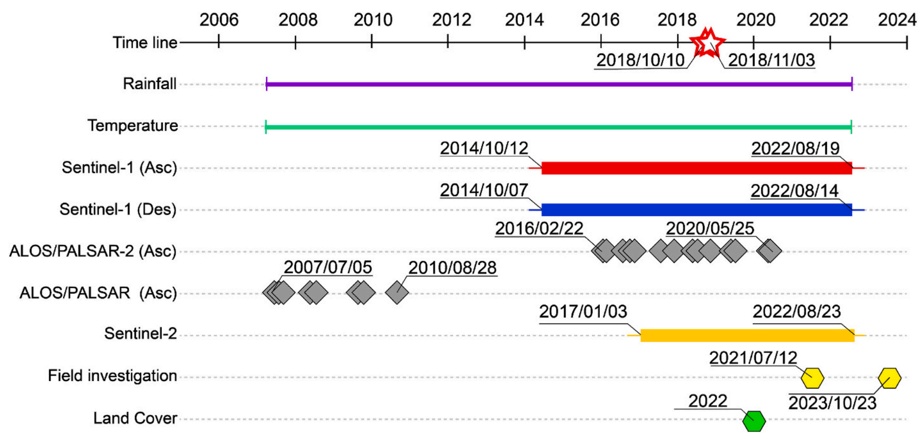


**Fig. 3.** Temporal coverage of datasets acquired over study area. The red five-pointed star marks the failure time of the Baige landslide. (For interpretation of the references to colour in this figure legend, the reader is referred to the web version of this article.)

**Table 1**
Parameters of satellite SAR datasets.

| Satellite | ALOS/ PALSAR | ALOS/ PALSAR-2 | Sentinel-1 | Sentinel-1 |
|---|---|---|---|---|
| Wavelength (m) | 0.236 | 0.236 | 0.056 | 0.056 |
| Orbit Direction | Ascending | Ascending | Ascending | Descending |
| Heading (°) | 349.70 | 349.65 | 347.25 | 192.74 |
| Incidence (°) at image center | 38.73 | 36.28 | 36.95 | 41.67 |
| Pixel size (m) (range×azimuth) | 9.36 × 3.17 | 4.29 × 3.78 | 2.3 × 14.0 | 2.3 × 14.0 |
| Multi-looking (range×azimuth) | 5 × 1 | 2 × 4 | 4 × 1 | 4 × 1 |
| Time Span (dd/mm/yyyy) | 05/07/2007–28/08/2010 | 22/02/2016–25/05/2020 | 12/10/2014–19/08/2022 | 07/10/2014–14/08/2022 |
| No. of images | 8 | 12 | 181 | 190 |
| No. of interferograms | 15 | 30 | 392 | 514 |

SAR data in both C-band and L-band to determine SSF and slide type, estimate landslide volume, and establish a long-time series of displacement (Fig. 4), which can be delineated into four sequential steps:

Step 1: Data input. This involves long-term, multi-orbit SAR data, multi-temporal satellite optical imagery, Generic Atmospheric Correction Online Service for InSAR (GACOS) products, and SRTM DEM data.

Step 2: Landslide detection. This step processes each SAR dataset individually to produce the annual surface deformation rate of the LOS direction and further integrate Google Earth satellite imagery and DEM to compile an inventory of landslides in the study area.

Step 3: Inversion of quasi-3D displacement, type and volume of active landslides. This step combines a topography-constrained model with multi-track InSAR observations to invert quasi-3D displacement. Subsequently, by assuming surface displacement parallel to the SSF, this step determines the LSSS and then assesses slide type and volume.

Step 4: Analyzing possible driving factors and kinematic behavior of active landslide. Employing the quasi-3D displacement field obtained in step 3, we calculate the SSF for each pixel of the landslide. Then, the Tikhonov regularization method is utilized to project LOS measurements from various SAR platforms onto the sliding surface direction of each landslide pixel, enabling the generation of long-term displacement time series. Subsequently, this study explores the triggering factors for landslide acceleration. Details of these methods are provided below:

### 3.1. Interferometric processing and time-series InSAR analysis

Using InSAR technology, each of the four SAR datasets underwent individual processing with GAMMA software (Wegnüller et al., 2016). SAR data processing involves five steps. First, SAR images of the same type were co-registered to a reference master image to generate interferograms, employing the parameter settings outlined in Table 1. Second, terrain phase removal, adaptive filtering and phase unwrapping (MCF) were performed on all interferograms (Chen and Zebker, 2000). External SRTM DEM and geometric parameters of the SAR system were then used to mask out areas with geometric distortion (shadows and layover) in the study area, enhancing computational efficiency. Third, GACOS was employed to remove atmospheric delay errors from each interferogram (Yu et al., 2018), resulting in a 57 % and 66 % reduction in standard deviation (SD) for ascending and descending Sentinel-1, respectively (Fig. 5). Notably, GACOS was not applied for atmospheric correction of the interferograms generated from ALOS/PALSAR-1 and ALOS/PALSAR-2 data in this study, as no significant atmospheric errors were observed in the acquired interferograms (Fig. S2). Fourth, a spatial-temporal Atmospheric Phase Screen filter was applied to further reduce the short wavelength atmospheric residual errors (Yu et al., 2020). Finally, we corrected DEM and orbit errors, manually selected interferograms with smaller SDs, as illustrated in Fig. 6. Annual surface displacement rates were measured using the InSAR stacking method (Chen et al., 2024; Xiao et al., 2022), and the displacement time series were estimated using the least squares inversion method (Berardino et al., 2002; Yu et al., 2020).

### 3.2. Slip surface inversion and volume estimation

Assuming that the surface displacement vector is parallel to the landslide SSF, Carter and Bentley (1985a, 1985b) inferred the SSF position from surface displacements and tested this method across various types of landslide models, finding that the accuracy could reach approximately 2 % of the distance between ground measurement points. Baum et al. (1998) further confirmed that the displacement of a point on the landslide surface is generally parallel to the SSF, except in cases where there is significant thickening or thinning of the landslide material. Therefore, under this assumption, landslide 3D displacements can be used to infer the SSF and estimate landslide volume.

Here we combine multi-track InSAR observations to determine landslide 3D displacements. The measurement results obtained by InSAR ($V_{los}$) are a projection of 3D displacements onto the LOS direction:

$$V_{los} = lX \tag{1}$$

where$l = [sin\theta sin\alpha \quad -sin\theta cos\alpha \quad cos\theta]$ and $X = [V_N \quad V_E \quad V_U]^T$. $\theta$ is the local incidence angle of the radar beam and $\alpha$ is the local heading angle of the satellite (clockwise from north as positive).

Due to the specific orbital path of SAR satellites (which typically

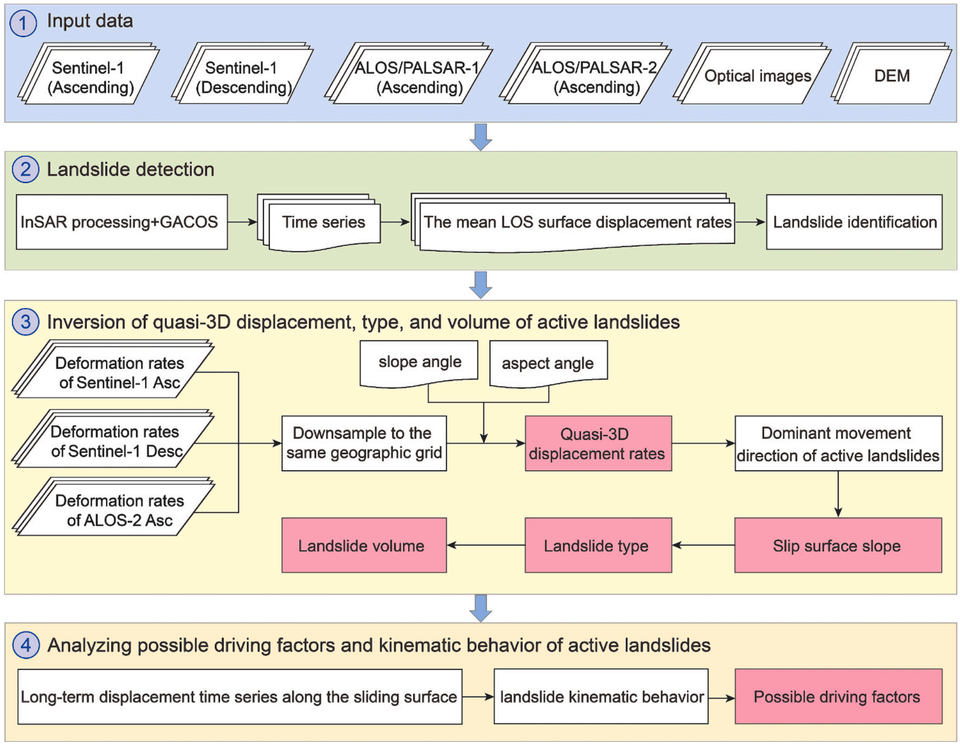


**Fig. 4.** Flow chart for landslide detection, slip surface geometry, volume estimation and kinematic behavior analysis.

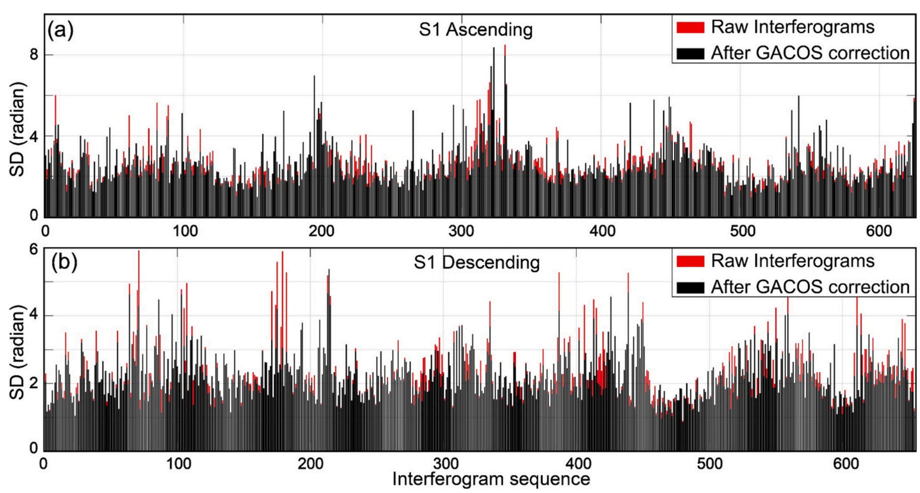


**Fig. 5.** SD of interferograms before and after atmospheric corrections. (a) and (b) represent ascending and descending Sentinel-1 datasets, respectively.

follow near-polar orbits), directly computing 3D displacement using the displacement outcomes from three LOS directions encounters a problem with rank deficiency. This issue makes the results unreliable (Hu et al., 2014). Considering the predominantly downslope movement characteristic of active landslides under the influence of gravity, in this study, a coordinate system $D_aD_bD_c$ is established along the slope surface of the landslide (Fig. 7). We assume that the displacement in the $D_b$ direction is zero. This assumption is generally valid, as demonstrated by Hu et al. (2018). Therefore, deformation in the N-S, *E*-W and vertical directions can be calculated using least squares as follows:

$$\begin{bmatrix} V_{los1} \\ V_{los2} \\ V_{los3} \\ 0 \end{bmatrix} = \begin{bmatrix} l_{los1} \\ l_{los2} \\ l_{los3} \\ S_b \end{bmatrix} \begin{bmatrix} V_N \\ V_E \\ V_U \end{bmatrix} \tag{2}$$

where $S_b$ represents the projection coefficient matrix of $D_b$. Here, $S_b = [\,sin\beta \quad -cos\beta \quad 0\,]$ and $\beta$ is the aspect angle.

Deformation in the coordinate system $D_aD_bD_c$ can be converted by eq. (3):

$$\begin{bmatrix} V_a \\ V_c \\ V_b \end{bmatrix} = s^T \begin{bmatrix} V_N \\ V_E \\ V_U \end{bmatrix} \tag{3}$$

where $s = \begin{bmatrix} cos_\beta cos_\delta & cos_\beta sin_\delta & sin_\beta \\ sin_\beta cos_\delta & sin_\beta sin_\delta & -cos_\beta \\ -sin_\delta & cos_\delta & 0 \end{bmatrix}$ and $\delta$is the slope angle.

After obtaining the 3D displacement, we employed the deformation in the $D_a$ and $D_c$ directions to infer the LSSS, using the following calculation formula:

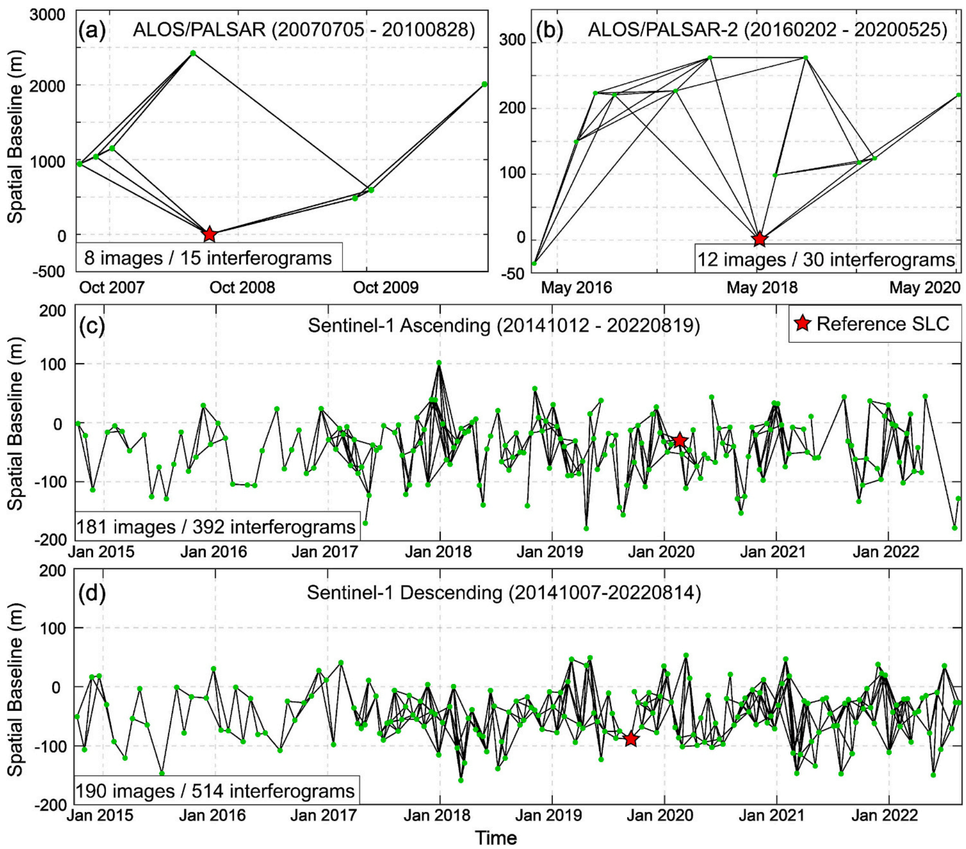


**Fig. 6.** Spatiotemporal baseline combinations of interferograms from (a) ALOS/PALSAR dataset; (b) ALOS/PALSAR-2 dataset; (c) ascending Sentinel-1 dataset; and (d) descending Sentinel-1 dataset.

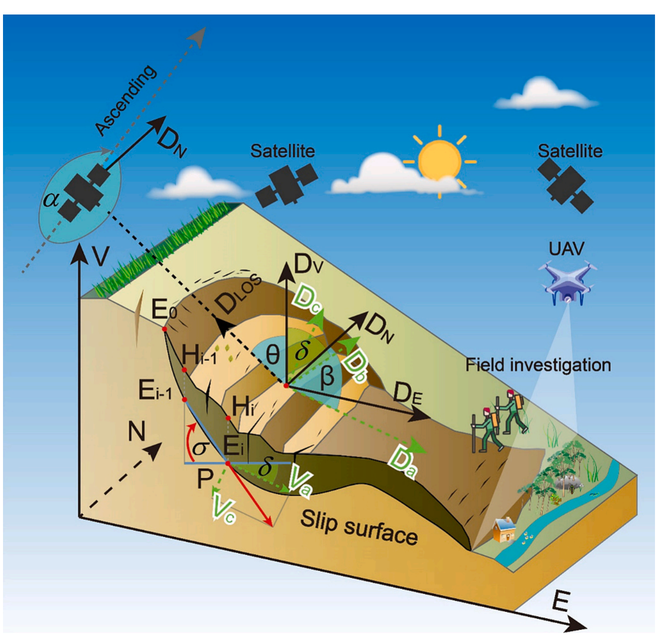


**Fig. 7.** InSAR landslide downslope displacement transformation model, where α is heading angle, θ is incidence, $\beta$ is aspect angle, $\delta$is slope angle and $\sigma$ is slip surface slope.

$$\sigma = \delta \pm arctan\left(\frac{V_c}{V_a}\right) \tag{4}$$

where $\delta$ indicates the slope angle (see Fig. 7) – if $V_c > 0$, it is negative and, if $V_c < 0$, it is positive.

The SD of the LSSS is evaluated according to the error propagation law:

$$m_\sigma^2 = \left(\frac{\partial_\sigma}{\partial_{V_c}}\right)^2 m_c^2 + \left(\frac{\partial_\sigma}{\partial_{V_a}}\right)^2 m_a^2 \tag{5}$$

where m indicates the SD.

After obtaining the LSSS, the altitude of the SSF is calculated by the elevation of the crown of the landslide and the LSSS:

$$E_i = E_{i-1} - p \times tan\sigma_i, \quad i \geqslant 1 \tag{6}$$

where $i$ represents a pixel unit on the SSF, $i-1$ represents the preceding unit from pixel $i$ along the SSF, $E_i$ represents the elevation of $i$, $\sigma_i$ denotes the LSSS of $i$ and $p$ is the horizontal distance in pixels (Fig. 7). It is noteworthy that $E_0$ represents the elevation value at the crown of the landslide.

The volume of the active landslide can be estimated using the following formula:

$$V = p\sum_{i=1}^{n}(H_i - E_i) \tag{7}$$

where $H_i$ represents the elevation at position $i$ on the landslide and $n$ denotes the number of pixels within the landslide boundary.

### 3.3. Determination of slide type

Hungr et al. (2013) classified landslides into five types: planar slides, rotational slides, wedge slides, compound slides and irregular slides. Due to the complexity of the SSF in wedge slides, compound slides and irregular slides, it is extremely challenging to determine this based on surface information alone. Therefore, we simplified the classification and primarily categorized landslides into rotational slides (RLs), planar slides (PLs) and complex slides (CLs). By considering the irregularity of landslide boundaries, we created a buffer along the landslide boundaries based on the outcomes of SSF angles perpendicular to the optimal sliding direction (Frattini et al., 2018). In this study, we computed the average angle of the SSF within the buffer zone using a buffer size of 50 m. Subsequently, each landslide is characterized by a LSSS profile along its optimal sliding direction, and the landslide movement type was determined based on the trend of this profile. Fig. 8 illustrates a detailed 3D schematic, showing side-view topographic profiles and LSSS variation for each slide type.

### 3.4. Estimation of long-term displacement time series along sliding surface

Understanding the movement mechanism of landslides using LOS deformation information and relatively short deformation time series (e.g., less than five years) is challenging. Therefore, based on the 3D displacement field, the sliding surface direction for each pixel of the landslide becomes crucial. By projecting LOS displacement information onto the sliding surface direction, we can reflect the true magnitude of the landslide movement, providing further insights into landslide dynamics. The formula for projecting LOS displacement values ($V_{los}$) onto the sliding surface direction ($V_{dslp}$) is as follows:

$$V_{dslp} = V_{los} / C \tag{8}$$

where $C$ is calculated as:

$$C = sin\theta cos\alpha cos\delta sin\beta - sin\theta sin\alpha cos\delta cos\beta + cos\theta sin\delta \tag{9}$$

It should be noted that the absolute value of the $C$ is greater than 0.3, to avoid anomalous exaggeration caused by projection (Herrera et al., 2013; Song et al., 2022).

Upon projecting LOS deformation details from the four data types onto the most suitable sliding direction, we employed a Tikhonov regularization technique (Liu et al., 2021; Tihonov, 1963) for the extended integration of these four data types. Finally, this procedure yielded the 15-year deformation history along the sliding surface for the LGGC.

## 4. Results and analysis

### 4.1. Mapping active landslides and stabilized paleo-landslides in LGGC

Because SAR operates in a side-looking imaging mode, it presents geometric alterations in specific areas within SAR images (Chen et al., 2022). Evaluating the suitability of SAR data is crucial before conducting landslide detection. To address this, we assessed the visualization results of the SAR data. The results demonstrated that the integration of four SAR datasets provided near-complete spatial coverage (92.66 % of the total study area, Fig. S3), significantly improving the detection capability for active landslides across the LGGC. To further validate the accuracy of the InSAR-derived deformation results, we employed both internal and external consistency methods. First, statistical analyses of the deformation fields derived from ALOS/PALSAR-1, ALOS/PALSAR-2, ascending Sentinel-1, and descending Sentinel-1 images indicated that each dataset follows a Gaussian distribution (Fig. 9e-h), with $R^2$ values exceeding 0.98. Fig. S4 presents the SD of LOS displacement rate maps from different SAR datasets, all within ±10 mm, demonstrating the millimeter-level precision of InSAR. Furthermore, we compared the InSAR deformation results with those obtained from a GNSS monitoring station located approximately 50 km from the study area. As shown in Fig. S5, the GNSS results are generally consistent with the InSAR observations (48-day time baseline). In conclusion, the InSAR deformation results obtained in this study are deemed reliable.

In this study, 53 landslides were detected by employing a combined approach of multi-scale and multi-temporal optical remote sensing interpretation techniques (Chen et al., 2022; Guzzetti et al., 2012), along with four LOS annual surface displacement velocities (Fig. 9). Among these, 37 were active landslides and 16 were stabilized paleo-landslides (Fig. 10). Table S1 presents detailed attributes of the landslides, with landslide areas ranging from 0.05 $km^2$ to 8.57 $km^2$. Notably, all the 53 landslides we detected have been validated through field survey (Fig. 2). Landslide boundaries were delineated based on four LOS annual surface

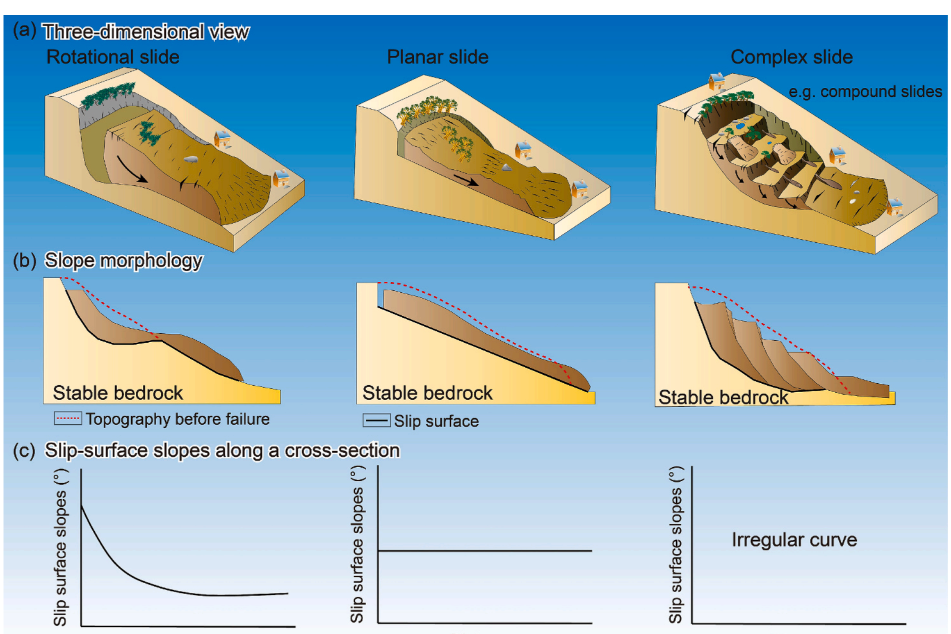


Fig. 8. Determining landslide type based on sliding surface angle (modified from Schlögel et al., 2015).

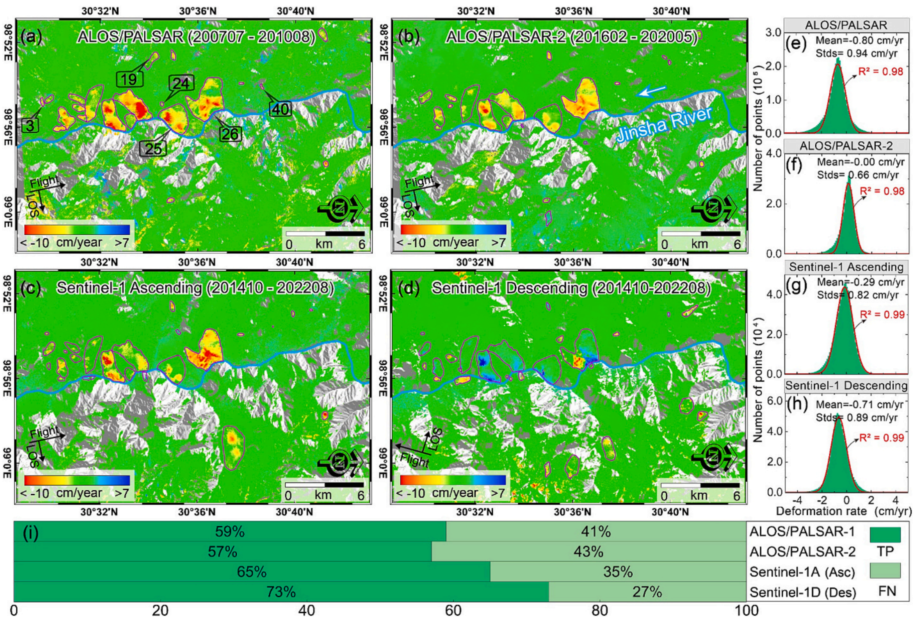

**Fig. 9.** LOS annual surface displacement rate maps for LGGC derived from (a) ascending ALOS/PALSAR, (b) ascending ALOS/PALSAR-2, (c) ascending Sentinel-1, and (d) descending Sentinel-1 images. Purple polygons mark active landslide boundaries. (e)-(h) show the corresponding deformation histograms, and (i) presents the accuracy of active landslide detection from different SAR images. (For interpretation of the references to colour in this figure legend, the reader is referred to the web version of this article.)

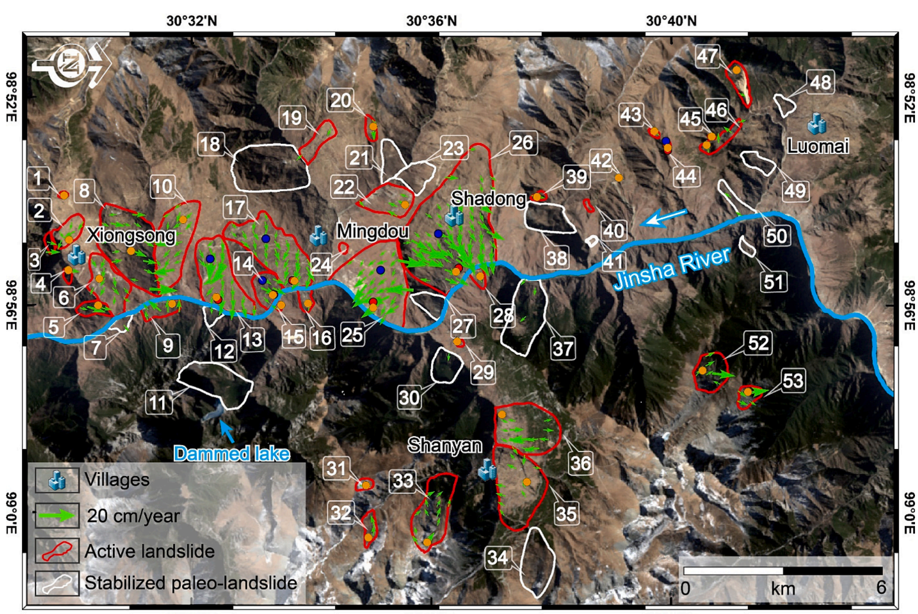

**Fig. 10.** Location, extent and horizontal movement vector of detected landslides. Numbers 1 to 52 indicate serial numbers of landslide. Red and blue dots represent foot and head spatial position of six landslide cases, respectively, for 15-year deformation history analysis (Fig. 14). Orange dots indicate the spatial locations of active landslide for temporal analysis (Fig. 16). (For interpretation of the references to colour in this figure legend, the reader is referred to the web version of this article.)

displacement rates and geomorphological features.

It is crucial to emphasize that different SAR datasets exhibit varied detection capabilities in the same region. Specifically, ALOS/PALSAR-1, ALOS/PALSAR-2, ascending Sentinel-1 and descending Sentinel-1 detected 22, 21, 24 and 27 active landslides, respectively. To evaluate the accuracy of landslide detection for each SAR dataset, we assessed True Positives (TP), False Positives (FP), and False Negatives (FN). The results indicate that descending Sentinel-1 achieved the highest TP rate at 73 %, while ALOS/PALSAR-2 recorded the highest FN rate at 43 % (Fig. 9i). Importantly, the FP rate for all four SAR datasets was 0, indicating no false detections. Furthermore, four landslides (Nos. 3, 19, 24 and 40) were active during 2006–2010 but stabilized between 2014 and 2022. The largest active landslide in the region is the Shadong landslide (No. 26), measuring 2130 m × 2680 m. Our detection results are consistent with those of Liu et al. (2021), Yan et al. (2024) and Yao et al. (2022), including landslides such as the Shadong (No. 26) and Sela (No. 25) landslides. However, 30 % of the landslides were not detected in previous studies (Table S1). There is a twofold explanation for our improved results: (1) the utilization of more detailed data, incorporating SAR data in both C-band and L-band from different orbits, as well as multi-temporal optical satellite imagery, and (2) the SAR images have a longer coverage period, spanning 2006–2010 and 2014–2022, and stabilized paleo-landslides were identified through visual interpretation of Google Earth images combined with DEM and Sentinel-2 data.

### 4.2. Quasi-3D displacement fields

The acquisition of quasi-3D displacement is a critical step in determining the optimal sliding direction and SSF of active landslides and calculating the LSSS with precision depends on the accuracy of 3D displacement. In this study, the quasi-3D displacement of LGGC was derived using the method described in Section 3.2, based on the LOS annual deformation rates (Fig. 9), satellite incidence and heading angles, as well as slope and aspect (Fig. S6). Fig. 11a-f show the quasi-3D displacement rates of LGGC in the N-S, *E*-W, vertical, downslope, normal to downslope and slope-normal directions from February 2016 to May 2020, respectively. Fig. S7a-f depict the corresponding SDs. The 3D displacement results for stabilized paleo-landslides show no displacement. In contrast, active landslides exhibit continuous spatial deformation patterns that align with the topographical features of the landslides. For instance, landslides with predominantly E-W movement exhibit only localized N-S displacement, which vertical deformation consistently shows subsidence, aligning perfectly with the geomorphic characteristic movement of landslides. Also, the landslide movement is oriented in the N-S direction and the SD of the active landslide is larger. This observation is notably visible in landslide Nos. 35 and 36 (Fig. S7).

### 4.3. Slip surface, type and volume of active landslides

Fig. 12 illustrates the LSSS and their corresponding SD for the LGGC. Landslides oriented in the N-S direction exhibit a larger SD (e.g., Nos. 35 and 36), primarily attributed to the lower accuracy in quasi-3D data acquisition. As an illustration, taking landslide Nos. 13, 14, 26 and 44 (Fig. 12c-f) as examples, we first determined the optimal sliding direction. Along this direction, we delineated a 50 m buffer zone and calculated the average LSSS within that buffer zone. Fig. 12g-j present each landslide profile graph. Integrating these profiles with the schematic diagram of the landslide movement pattern in Section 3.3 (Fig. 7), we observe that the sliding surface angle profiles of landslide Nos. 13 and 26 correspond with the CLs (Fig. 7g and i), the profile of landslide No. 14 aligns with the PLs (Fig. 7h) and the profile of landslide No. 44 corresponds with the RLs (Fig. 7j). Upon evaluating all landslides in the LGGC, it is clear that the predominant landslide movement pattern in this study area is CL, encompassing five RLs, three PLs and 20 CLs (Table S1).

Fig. S8 illustrates the SSF depths for each active landslide in the LGGC, with the maximum SSF depth reaching 114 m for landslide No. 53. The minimum landslide volume is $1.66 \times 10^5$ $m^3$ (No. 42). The maximum landslide volume is $1.72 \times 10^8$ $m^3$ (No. 35). To validate the reliability of our calculated results, we compared the InSAR-derived SSF with independent in-situ measurements (ERT and boreholes) of the SSF in landslides Nos. 25 and 26 (Fig. 13). For landslide No. 25, the ERT

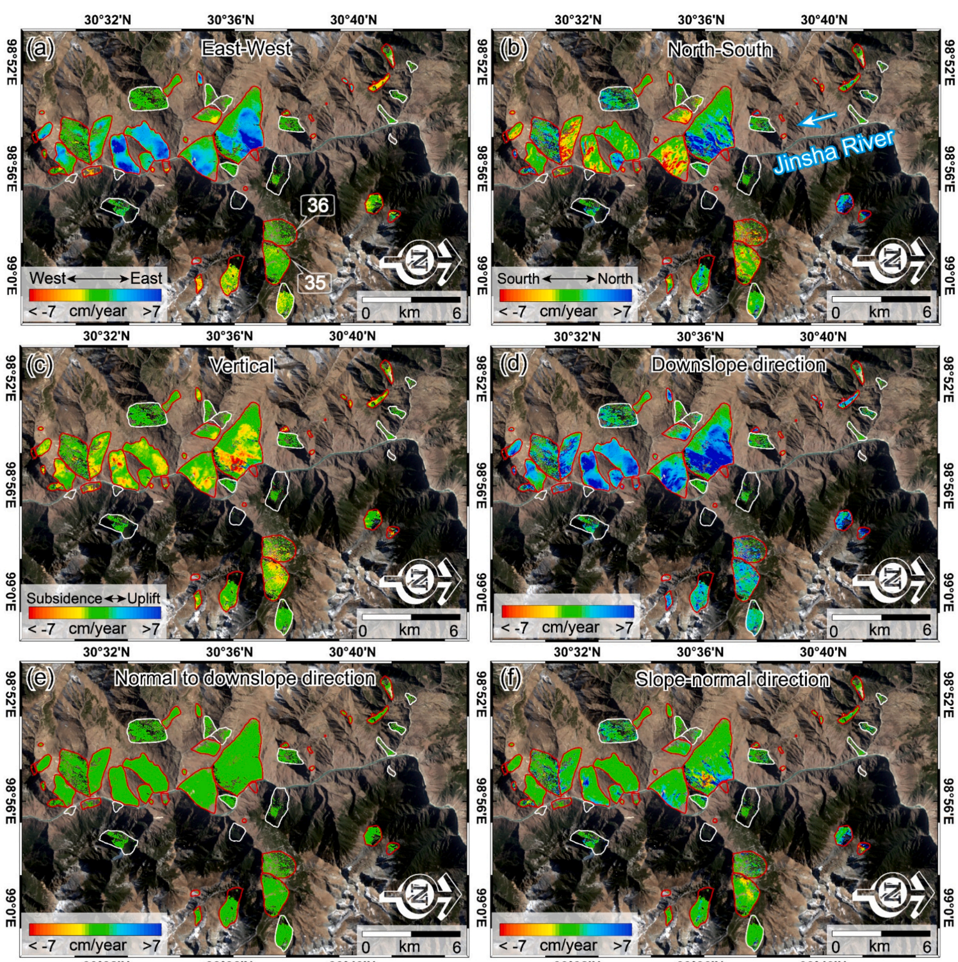


**Fig. 11.** Quasi-3D displacement of LGGC: (a) E-W deformation, (b) N-S deformation, (c) vertical deformation, (d) downslope direction displacement, (e) normal to downslope direction displacement (Note: assumption in this study is that displacement in this direction equals zero), and (f) slope-normal direction displacement.

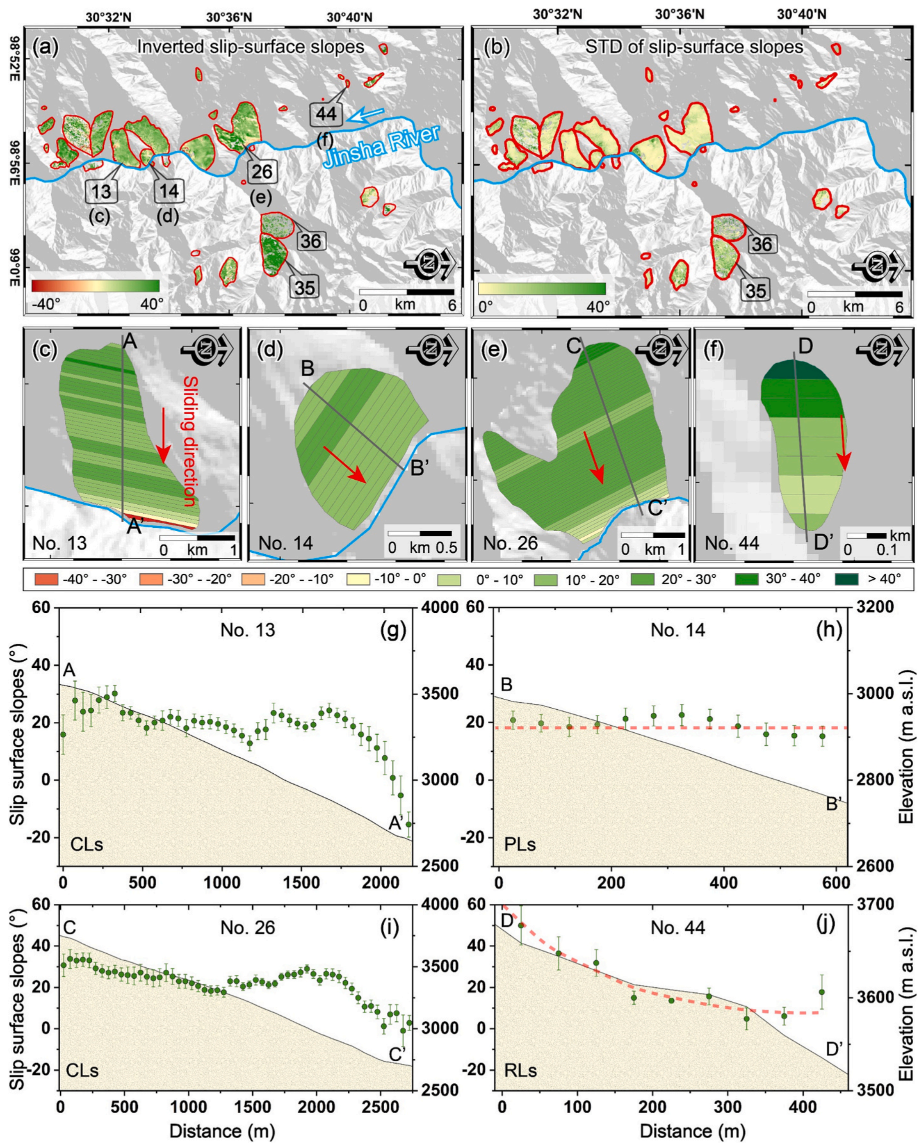

**Fig. 12.** (a) Slip surface slopes; (b) SD of slip surface slopes; (c-d) longitudinal swath profile, colour-coded based on mean slip surface slopes of landslide Nos. 13, 14, 26 and 44; and (g-j) cross-sections of terrain and slip surface slopes for landslide Nos. 13, 14, 26 and 44. The red dashed line is the fitted curve. (For interpretation of the references to colour in this figure legend, the reader is referred to the web version of this article.)

results indicate multiple SSFs, with the InSAR-inferred SSF closely matching those shown by ERT. For landslide No. 26, two boreholes were available, located on different cross-sections, so we compared the SSF in each respective section. Field photographs of the core samples reveal that this section of the core has a high water content, finer-grained material, and exhibited a sudden increase in drilling speed (Fig. 13). The SSF depths estimated in this study are consistent with borehole data, differing by only 0.8 m to 6.25 m (Fig. 13). Additionally, we referred to the existing landslide research literature for this region. The volume measurements we computed for active landslides were consistent with the values reported in the existing literature, falling within a similar range of magnitude (Table 2). However, the volume results in this study are somewhat smaller in comparison. We attribute this phenomenon to the fact that, during volume calculations, we used the boundaries representing the extent of surface displacement (i.e., the active part of the landslides). In contrast, the volumes recorded in the literature are based on the entire topographical range of the landslide. Moreover, literature-recorded results may still require correction. For example, the volume of the landslide No. 25 was obtained through a single profile geophysical survey (Yan et al., 2024; Zhu et al., 2021), while that of landslide No. 26 was deduced from two borehole data (Li et al., 2021). Another contributing factor to the observed differences is the inherent limitation of our research methodology, which can only capture one sliding surface for an active landslide. It should be noted that our approach is unable to address landslides with multiple sliding surfaces. This limitation reflects the inherent constraints of obtaining deep-seated data for landslides using a 3D displacement field.

### *4.4. 15-year deformation history and potential driving factors of LGGC*

To gain a comprehensive understanding of the long-term kinematic behaviors of landslides, we merged ALOS/PALSAR and Sentinel-1 data following the methodology outlined in Section 3.4, thereby capturing 15 years of surface displacement along the sliding surface from July 2007 to August 2022 for the LGGC. It is important to note a data gap spanning four years (September 2010 to September 2014). To ensure data reliability, this study extracted the mean deformation within the 100 m × 100 m range of the foot and head of CL (Nos. 13, 17, 25 and 26), PLs (No. 14) and RL (No. 44) landslides, as illustrated in Fig. 14. Over the past 15 years, landslide Nos. 13, 14, 17, 25, 26 and 44 have displayed

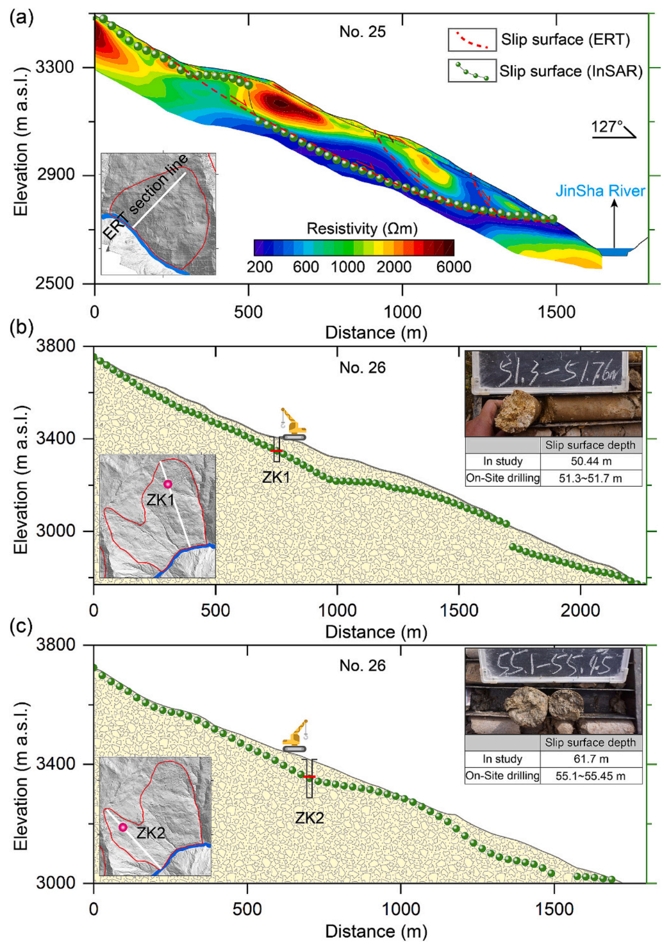


**Fig. 13.** Validation of the inferred landslide slip surface (SSF) depth. (a) Geophysical profile of the Sela landslide (resistivity adapted from Zhu et al., 2021). (b-c) Cross-sections of the Shadong landslide, with borehole data from Li et al., 2021. Black rectangles indicate boreholes; red solid lines show SSF from borehole interpretation. Cross-section locations are shown in the lower-left inset. (For interpretation of the references to colour in this figure legend, the reader is referred to the web version of this article.)

**Table 2**
Volume of active landslides, derived from this study and previous research.

| Number | Landslide Name | Volume | |
|---|---|---|---|
| | | In this study | Geological survey |
| No. 25 | Sela | $5.0 \times 10^7$ m$^3$ | $6.52 \times 10^7$ m$^3$ (Zhu et al., 2021)<br>$1.8 \times 10^8$ m$^3$ (Yan et al., 2024) |
| No. 26 | Shadong | $1.22 \times 10^8$ m$^3$ | $2.6 \times 10^8$–$6.0 \times 10^8$ m$^3$ (Li et al., 2021)<br>$0.5 \times 10^8$ m$^3$ (Yao et al., 2022) |

displacements of 1.37, 0.7, 0.75, 0.77, 1.42 and 0.94 m, respectively. An analysis of movement trends at the foot and head of three types of landslide show RLs and PLs to exhibit a similar deformation pattern at the foot and head (Fig. 14b and f). In contrast, due to the movement complexity of CLs, variety is evident in the movement at the foot and head (e.g., consistency in Fig. 14d and e and inconsistency in Fig. 14a and c).

Fig. 14 indicates a significant displacement acceleration signal in November 2018 coincident with the timing of the Baige landslide. The Baige landslide is located approximately 50 km upstream from the study area. The first landslide event occurred on 10 October 2018, blocking the Jinsha River and forming a landslide dam. The dam created a lake with a water level of approximately 36.4 m and a storage capacity of around $2.9 \times 10^8$ m$^3$. The lake began to discharge naturally on 12 October with the process concluding by 13 October 2018. The second event occurred on 3 November 2018, resulting in a new landslide dam. This second lake reached a water level of up to 50 m, with a storage capacity exceeding $5 \times 10^8$ m$^3$. After engineering interventions, discharge began on 12 November, and the water levels upstream and downstream of the dam were fully connected by 13 November 2018 (Fan et al., 2019). To investigate whether the acceleration signal was influenced by external triggering factors such as earthquakes, rainfall, and snowmelt, we first collected seismic catalog data from October to November 2018 (Fig. S9). We found that the closest earthquake greater than Mw 4.0 during this period occurred at a distance of 370 km from our study area, indicating that the acceleration of the LGGC was not affected by seismic activity according to previous studies about earthquake induced landslides (David, 1984). Secondly, there was no recorded heavy rainfall in the study area from October to November 2018 (Fig. 14), while rules out the influence of rainfall. Furthermore, as this period did not fall within the snowmelt season in the study area, the impact of snowmelt was also excluded. This acceleration signal persisted, indicating a lasting acceleration effect on the LGGC resulting from the breach of the Baige landslide dam, as discussed further in Section 5.2. Apart from the accelerations during these two major events, landslide movements were not linear but exhibited localized accelerating signals, typically associated with periods of intense rainfall (indicated by the black arrow in Fig. 14). This signifies that rainfall also contributes to accelerated movements within the LGGC.

## 5. Discussion

### 5.1. Impact of DEM on quasi-3D displacement and volume estimation

In the computation of quasi-3D displacement for landslides using terrain-constrained models, accuracy of the slope and aspect data is crucial. These parameters directly influence the outcomes of 3D displacement, subsequently affecting the inversion results of landslide SSF and volume. This research employed DSM acquired via UAV on 12 July 2021 as the DEM for landslide Nos. 25 and 26. It is noteworthy that the slopes of these landslides are primarily covered with grass (Fig. 2c). Therefore, we assumed that the DSM was equivalent to the DEM in this region. Applying the methodology outlined in Section 3.2.1, we calculated the deformation in directions Da, Db and Dc for landslide Nos. 25 and 26 using the slope and aspect derived separately from UAV DSM and SRTM DEM (Fig. 15a-f). The 3D displacement results obtained from SRTM DEM and UAV DSM exhibited a high degree of consistency, as illustrated by the subtraction of the two sets of results depicted in Fig. 15g-i. Remarkably, over 86 % of pixel points fell within the range of −1 to 1 cm. Anomalies were predominantly observed in localized areas characterized by complex terrain and topographical changes, such as newly formed gullies. Finally, the use of SRTM DEM is deemed sufficient for the inversion of the 3D displacement field, albeit with possible greater errors in regions with recent changes and intricate terrain.

The accuracy of landslide volume estimation is highly dependent on the precision of the DEM. To evaluate this dependency, we selected landslides Nos. 25 and 26 as examples. Landslide volume derived from UAV DSM was employed as a reference to validate the accuracy of volume estimates obtained from the SRTM DEM. The results show that the volume of landslide No. 25 estimated from the SRTM DEM is $7.07 \times 10^4$ m$^3$, larger than that estimated from the UAV DSM, with an error accounting for only 0.14 % of the landslide volume. Similarly, the volume of landslide No. 26 estimated from the SRTM DEM is $5 \times 10^5$ m$^3$, also larger than that estimated from the UAV DSM, but with an error of only 0.41 %. Therefore, the errors inherent in the SRTM DEM are not evident for landslide volume estimation. However, it is important to note that this study only compared two active landslides, which may not represent the broader context due to the limited sample size. We thus

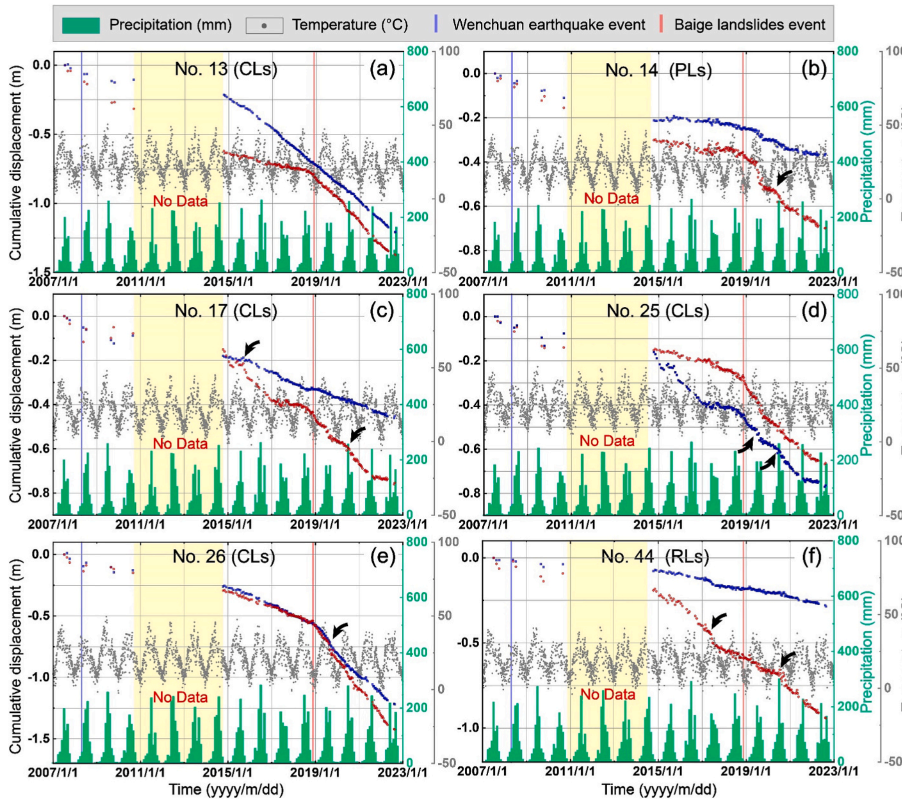


**Fig. 14.** Fifteen-year deformation along slip surface of landslide Nos. 13 (a); 14 (b); 17 (c); 25 (d); 26 (e); and 44 (f). Blue and red curves, respectively, represent different parts of landslide (Fig. 10). The black arrows indicate points of deformation acceleration caused by rainfall. (For interpretation of the references to colour in this figure legend, the reader is referred to the web version of this article.)

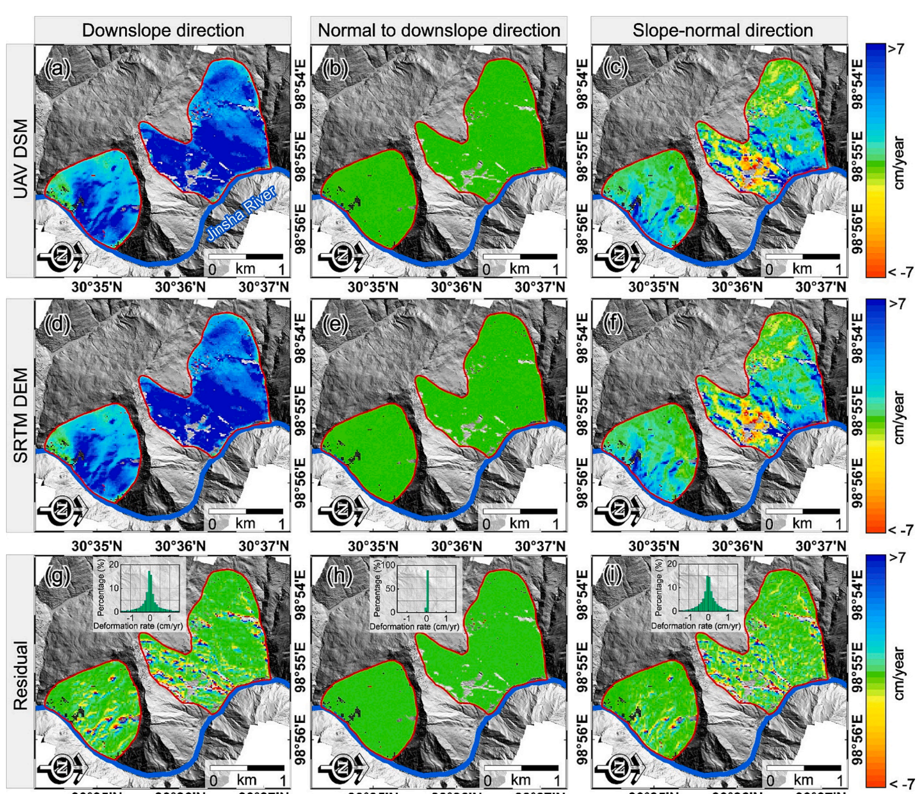


**Fig. 15.** (a-c) 3D displacement results constrained by UAV DSM; (d-f) 3D displacement results constrained by SRTM DEM; and (g-i) differences obtained by subtracting (a) from (d), (b) from (e), and (c) from (f). The base map is shaded image generated from DSM acquired by UAV on 12 July 2021.

recommend prioritizing higher-precision DEM for the estimation of landslide volume when possible.

### 5.2. Impact of flood disasters due to Baige landslide dam break on LGGC

To investigate the impact of the breach of the Baige landslide dam on LGGC, this study categorized landslides into wading landslides and non-wading landslides. Among these are nine wading active landslides and 28 non-wading active landslides. It is important to note that the determination of wading landslides was based on whether the deformation boundary of a landslide intersects with the Jinsha River. Average time series within a 100 × 100 m range around each landslide point are presented in Fig. 16. Interestingly, seven wading landslides exhibited clear acceleration signals following the occurrence of the Baige landslide (Fig. S10), while non-wading landslides exhibited no such signals. It should be noted that the two remaining wading landslides failed to capture this acceleration signal because of geometric distortions and directional limitations. The sliding direction of wading landslide No. 15 is almost parallel to the descending satellite orbit, with a deviation of only 20°, and it appears to be incoherent in the ascending orbit image. With landslide No. 28, the sliding direction deviated by 30° from the descending satellite orbit, presenting a challenge for the descending data to capture the accelerated displacement signal, as the ascending data was situated in a geometric distortion zone. When comparing Sentinel-2 false-colour images from 2017 to 2022 (Fig. S11), we observed that the first breach of the Baige landslide dam resulted in relatively minor erosion within LGGC. However, the dam formed after the second Baige landslide had a pronounced erosive impact on the toe of LGGC, resulting in substantial collapses at the maximum length of 125 m (Fig. S12). This alteration affected the stress distribution at the base of wading

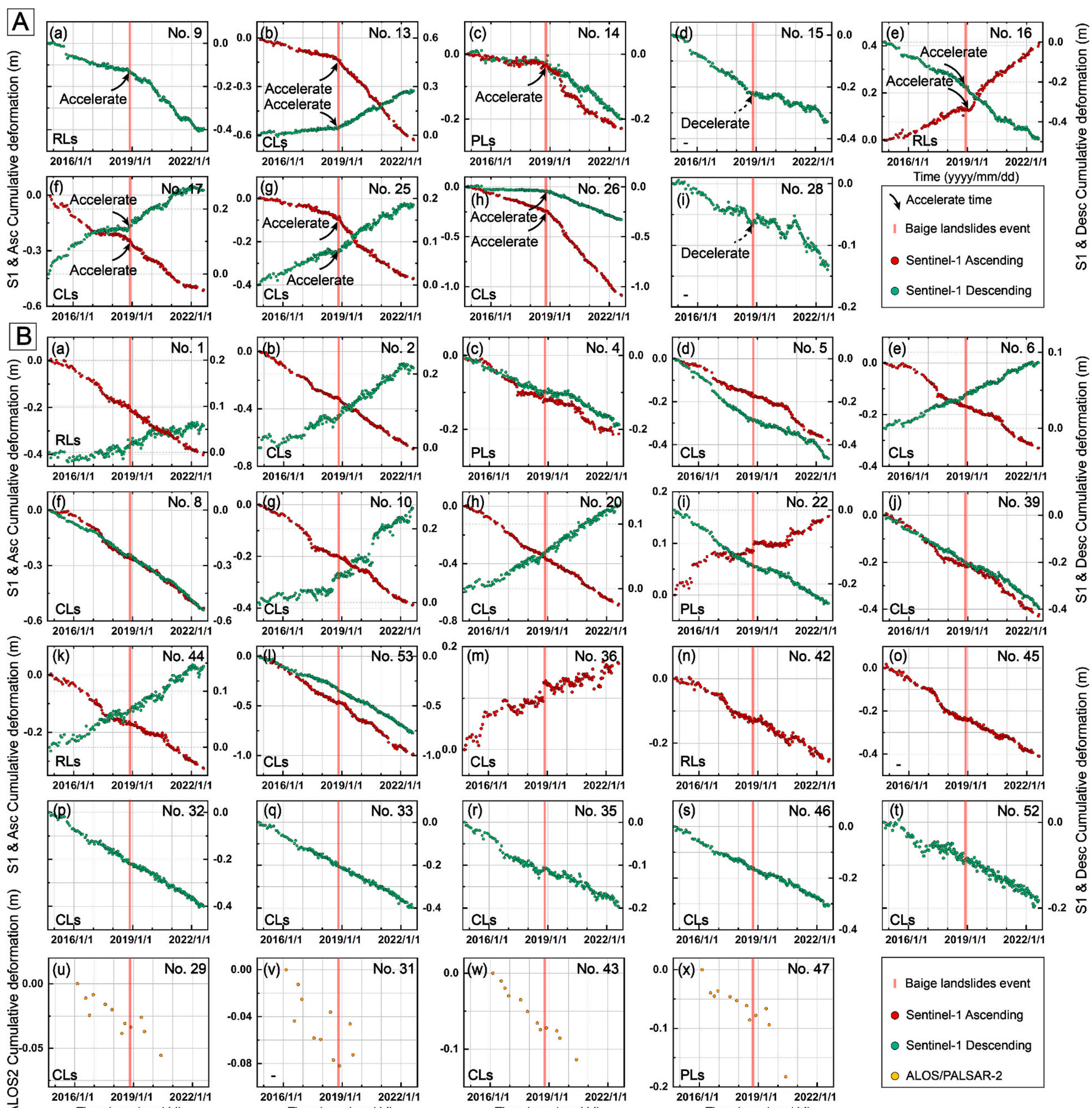


**Fig. 16.** LOS displacement time series of all 33 detected active landslides for period October 2014 to September 2022. (a) Wading landslides, (b) Non-wading landslides.

landslides, causing significant and permanent acceleration.

### 5.3. Surface area-volume relationship of landslide

The estimation of landslide volume is crucial for the assessment of landslide hazards. Previous studies have revealed that the surface area (A) and volume (V) of landslides triggered by different mechanisms in different regions appear to follow a power-law function (i.e., $V = c \times A^{\varepsilon}$), where $c$ is a constant. The power-law function relationship between the surface area and volume of 25 active landslides in the LGGC is derived by $V = 26.26 \times A^{0.98}$. Comparing the volume-area relationships attained for active landslides in this study with existing research (as shown in Table S2 and Fig. 17), it is observed that the volumes of active landslides estimated in this study exhibit good consistency with the existing power functions. It is important to note that, due to the limited number of landslides in our dataset, the power functions obtained in this study are applicable only for estimating landslide volumes within the range of active landslide areas from $6.46 \times 10^3$ m$^2$ to $5.88 \times 10^6$ m$^2$.

### 5.4. Comparative analysis of landslide slip surface estimation methods

Although various methods for estimating landslide SSF and volumes based on ground surface deformation have been developed in the past, such as the elastic dislocation method (Aryal et al., 2015) and the mass conservation method (Hu et al., 2018), their applicability is often constrained by model assumptions, making it challenging to extend these approaches to large-scale landslide studies (Table 3). Specifically, the elastic dislocation method, based on elastic mechanics theory, estimates the depth of the basal failure surface using landslide topographic and ground surface displacement, thereby deriving the SSF profile and landslide volume. However, its applicability is limited to the incipient stage of a landslide or cases without significant inelastic displacement, as the assumption of elasticity is often unrealistic in most landslide scenarios (Aryal et al., 2015; Saroli et al., 2021). The mass conservation method establishes a mathematical relationship between ground surface displacement and SSF depth based on pre-defined rheological laws. By utilizing a known 3D deformation, maximum SSF depth and landslide boundary, it estimates the SSF geometry (Hu et al., 2018). However, this method has several limitations: (1) it relies on an empirically predefined rheological parameter $f$, which is highly sensitive and will cause bias in landslide thickness estimation; (2) it requires prior knowledge of the maximum landslide thickness; and (3) it depends on well-defined constraints such as constant density and mass incompressibility.

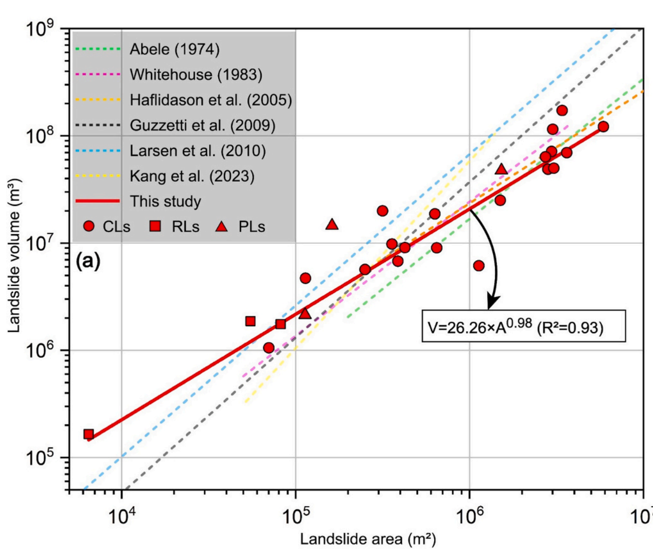


**Fig. 17.** Empirical relationship between volume and area of 25 active landslides along Jinsha River (Fig. 10), and area-volume power law from various authors (Abele, 1974; Guzzetti et al., 2009; Haflidason et al., 2005; Kang et al., 2023; Larsen et al., 2010; Whitehouse, 1983).

**Table 3**
Summary of methods for determining landslide slip surfaces using ground surface displacement.

| Method | Required Data | Output Results | Limitations |
|---|---|---|---|
| Elastic dislocation | DEM; Ground surface displacement | Longitudinal cross section of landslide sliding surface; Volume | Limited to the incipient stage of landslides or absence of significant inelastic displacement |
| Mass conservation | DEM, 3D-displacement; Rheological parameter f; Maximum landslide thickness | Landslide sliding surface; Volume | Limited by the rheological parameter f; Requires known maximum landslide thickness |
| In this study (Quasi-3D SSF Inversion Method) | DEM; 3D-displacement | Landslide sliding surface; Volume; Movement type | / |

In this study, we adopted a widely recognized and validated assumption that ground surface displacement vectors are parallel to the landslide SSF (Baum et al., 1998). By directly infer the LSSS from quasi-3D displacement, we reconstructed the spatial morphology of the SSF, estimated the landslide volume, and classified slide types. This approach is applicable to all types of landslides, enabling large-scale SSF estimation. The SSF results obtained for the Sela landslide (No. 25) and the Shadong landslide (No. 26) are generally consistent with ERT and borehole measurements, confirming the reliability of the proposed method. Nevertheless, it is important to note that existing inversion methods based on ground surface displacement can only effectively identify the SSF of active landslide bodies but are unable to infer the SSF of inactive landslides. Additionally, these methods are not suitable for complex landslides with multiple sliding surfaces. It is also noteworthy that InSAR technology remains limited by several factors, including phase decorrelation, phase unwrapping errors, atmospheric effects, and geometric distortions, which pose challenges in acquiring reliable ground surface displacement in certain regions. In these areas, complementary techniques, such as SAR/optical pixel offset tracking, DEM Differencing, and ground-based radar, can be employed to obtain surface displacement and support the estimation of landslide sliding surfaces.

## 6. Conclusion and limitations

In this study, we have proposed a comprehensive strategy for determining key parameters of active landslides, including SSF, volume, slide type and long-term deformation evolution. Our approach relies on multi-track and long-term SAR datasets, facilitating the calculation of crucial parameters for active landslides across a wide area. First, we generated annual surface displacement rates and LOS time series from four types of SAR data spanning from 2007 to 2022. Integrating InSAR displacement results from different periods and SAR datasets with optical remote sensing images, 53 landslides have been detected. Notably, this result aligns perfectly (100 %) with field campaigns. Second, the estimated 3D displacement field for LGGC, under the premise of a terrain-constrained model, allows the determination of the optimal sliding direction for every pixel within the landslide body. Third, we computed the SSF, slide type and volume of 37 active landslides. The findings revealed that the LGGC area is predominantly composed of CLs, with the deepest SSF reaching a depth of 114 m and volumes ranging from $1.66 \times 10^5$ m$^3$ to $1.72 \times 10^8$ m$^3$. Comparisons with independent in-situ measurements and existing literature support the reliability of the

SSF and volume estimates in this study. Fourth, long-term displacement of the sliding surface direction of LGGC over 15 years is generated, revealing a maximum displacement of 1.5 m. Notably, we observed a permanent acceleration effect on wading landslides in LGGC following the breach of the Baige landslide dam.

Finally, it is important to note that the comprehensive strategy proposed in this study relies on the quasi-3D deformation field of landslides and is applicable to active landslides with a single SSF. It is not suitable for active landslides with multiple SSF or inactive landslides. In conclusion, the novel approach presented in this study can calculate key parameters of landslides and attain information such as boundary, SSF, slide type, volume and long-term displacement of active landslides, providing valuable insights into landslide kinematics mechanisms. It also contributes to improve landslide risk assessment and management.

## CRediT authorship contribution statement

**Bo Chen:** Writing – original draft, Visualization, Validation, Software, Methodology, Investigation, Formal analysis, Data curation. **Zhenhong Li:** Writing – review & editing, Supervision, Resources, Project administration, Methodology, Funding acquisition, Conceptualization. **Chuang Song:** Writing – review & editing, Supervision, Methodology, Funding acquisition, Formal analysis, Conceptualization. **Chen Yu:** Writing – review & editing, Supervision, Software, Methodology. **Roberto Tomás:** Writing – review & editing, Supervision, Methodology, Funding acquisition. **Jiantao Du:** Methodology, Data curation. **Xinlong Li:** Investigation, Data curation. **Adrien Mugabushaka:** Writing – review & editing. **Wu Zhu:** Supervision, Resources. **Jianbing Peng:** Supervision, Resources.

## Declaration of competing interest

The authors declare that they have no known competing financial interests or personal relationships that could have appeared to influence the work reported in this study.

## Acknowledgements

This research was funded by the National Natural Science Foundation of China (Refs. 41941019 and 42304029), the Shaanxi Province Science and Technology Innovation Team (2021TD-51), the Shaanxi Province Geoscience Big Data and Geohazard Prevention Innovation Team (2022), the Fundamental Research Funds for the Central Universities, CHD (Refs. 300102264718, 300102261308 and 300102264302), the China Postdoctoral Science Foundation (Ref. 2024T170759), the Conselleria de Innovación, Universidades, Ciencia y Sociedad Digital in the framework of Project CIAICO/2021/335, the ESA-MOST China DRAGON-5 project (Grant No. 59339) and DRAGON-6 project (Grant No. 95355). This research was also supported by a Chinese Scholarship Council studentship awarded to Bo Chen (Ref. 202406560008). We would like to thank Researcher Sainan Zhu from the China Institute of Geological Environment Monitoring for providing the ERT results of the Sela landslide (No. 25).

## Appendix A. Supplementary data

Supplementary data to this article can be found online at https://doi.org/10.1016/j.rse.2025.114763.

## Data availability

Data will be made available on request.

## References

Abele, G., 1974. Bergsturze in Den Alpen ihre verbreitung, morphologie und folgeerscheinungen. Wiss. Alpenvereinshefte 25 (230p).

Aryal, A., Brooks, B.A., Reid, M.E., 2015. Landslide subsurface slip geometry inferred from 3-D surface displacement fields. Geophys. Res. Lett. 42, 1411–1417. https://doi.org/10.1002/2014GL062688.

Baum, R.L., Messerich, J., Fleming, R.W., 1998. Surface deformation as a guide to kinematics and three-dimensional shape of slow-moving, clay-rich landslides, Honolulu. Hawaii. Environ. Eng. Geosci. 4 (3), 283–306. https://doi.org/10.2113/gseegeosci.IV.3.283.

Berardino, P., Fornaro, G., Lanari, R., Sansosti, E., 2002. A new algorithm for surface deformation monitoring based on small baseline differential SAR interferograms. IEEE Trans. Geosci. Remote Sens. 40, 2375–2383. https://doi.org/10.1109/TGRS.2002.803792.

Carter, M., Bentley, S.P., 1985a. The geometry of slip surfaces beneath landslides: predictions from surface measurements. Can. Geotech. J. 22, 234–238. https://doi.org/10.1139/t86-012.

Carter, M., Bentley, S.P., 1985b. A procedure to locate slip surfaces beneath active landslides using surface monitoring data. Comput. Geotech. 1, 139–153. https://doi.org/10.1016/0266-352X(85)90032-1.

Chen, C.W., Zebker, H.A., 2000. Network approaches to two-dimensional phase unwrapping: intractability and two new algorithms. J. Opt. Soc. Am. 17, 401–414. https://doi.org/10.1364/JOSAA.17.000401.

Chen, B., Li, Z.H., Zhang, C.L., Ding, M.T., Zhu, W., Zhang, S.C., Han, B.Q., Du, J.T., Cao, Y.B., Zhang, C., Liao, Z.Y., Zhou, S.K., Wang, J.W., Peng, J.B., 2022. Wide area detection and distribution characteristics of landslides along Sichuan expressways. Remote Sens. 14 (14), 3431. https://doi.org/10.3390/rs14143431.

Chen, B., Li, Z.H., Song, C., Yu, C., Zhu, W., Liu, Z.J., Han, B.Q., Du, J.T., Zhang, C.L., Xu, F., Peng, J.B., 2024. Automatic detection of active geohazards with millimeter-to-meter-scale deformation and quantitative analysis of factors influencing spatial distribution: a case study in the Hexi corridor, China. Int. J. Appl. Earth Obs. Geoinf. 131, 103995. https://doi.org/10.1016/j.jag.2024.103995.

Crippa, C., Valbuzzi, E., Frattini, P., Crosta, G.B., Spreafico, M.C., Agliardi, F., 2021. Semi-automated regional classification of the style of activity of slow rock-slope deformations using PS InSAR and SqueeSAR velocity data. Landslides 18, 2445–2463. https://doi.org/10.1007/s10346-021-01654-0.

David, K.K., 1984. Landslides caused by earthquakes. GSA Bull. 95 (4), 406–421 doi:10.1130/0016-7606(1984)95<406:LCBE>2.0.CO;2.

Fan, X.M., Xu, Q., Alonso-Rodriguez, A., Subramanian, S.S., Li, W.L., Zheng, G., Dong, X. J., Huang, R.Q., 2019. Successive landsliding and damming of the Jinsha River in eastern Tibet, China: prime investigation, early warning, and emergency response. Landslides 16, 1003–1020. https://doi.org/10.1007/s10346-019-01159-x.

Frattini, P., Crosta, G.B., Rossini, M., Allievi, J., 2018. Activity and kinematic behaviour of deep-seated landslides from PS-InSAR displacement rate measurements. Landslides 15, 1053–1070. https://doi.org/10.1007/s10346-017-0940-6.

Funk, C., Peterson, P., Landsfeld, M., Pedreros, D., Verdin, J., Shukla, S., Husak, G., Rowland, J., Harrison, L., Hoell, A., Michaelsen, J., 2015. The climate hazards infrared precipitation with stations – a new environmental record for monitoring extremes. Sci Data 2, 150066. https://doi.org/10.1038/sdata.2015.66.

Guzzetti, F., Ardizzone, F., Cardinali, M., Rossi, M., Valigi, D., 2009. Landslide volumes and landslide mobilization rates in Umbria, Central Italy. Earth Planet. Sci. Lett. 279, 222–229. https://doi.org/10.1016/j.epsl.2009.01.005.

Guzzetti, F., Mondini, A.C., Cardinali, M., Fiorucci, F., Santangelo, M., Chang, K.T., 2012. Landslide inventory maps: new tools for an old problem. Earth Sci. Rev. 112, 42–66. https://doi.org/10.1016/j.earscirev.2012.02.001.

Haflidason, H., Lien, R., Sejrup, H.P., Forsberg, C.F., Bryn, P., 2005. The dating and morphometry of the Storegga slide. Mar. Pet. Geol. 22, 123–136. https://doi.org/10.1016/j.marpetgeo.2004.10.008.

Handwerger, A.L., Roering, J.J., Schmidt, D.A., Rempel, A.W., 2015. Kinematics of earthflows in the northern California coast ranges using satellite interferometry. Geomorphology 246, 321–333. https://doi.org/10.1016/j.geomorph.2015.06.003.

Herrera, G., Gutiérrez, F., García-Davalillo, J.C., Guerrero, J., Notti, D., Galve, J.P., Fernández-Merodo, J.A., Cooksley, G., 2013. Multi-sensor advanced DInSAR monitoring of very slow landslides: the Tena Valley case study (central Spanish Pyrenees). Remote Sens. Environ. 128, 31–43. https://doi.org/10.1016/j.rse.2012.09.020.

Hu, J., Li, Z.W., Ding, X.L., Zhu, J.J., Zhang, L., Sun, Q., 2014. Resolving three-dimensional surface displacements from InSAR measurements: a review. Earth Sci. Rev. 133, 1–17. https://doi.org/10.1016/j.earscirev.2014.02.005.

Hu, X., Lu, Z., Pierson, T.C., Kramer, R., George, D.L., 2018. Combining InSAR and GPS to determine transient movement and thickness of a seasonally active low-gradient translational landslide. Geophys. Res. Lett. 45, 1453–1462. https://doi.org/10.1002/2017GL076623.

Hungr, O., Leroueil, S., Picarelli, L., 2013. The Varnes classification of landslide types, an update. Landslides 11, 167–194. https://doi.org/10.1007/s10346-013-0436-y.

Intrieri, E., Frodella, W., Raspini, F., Bardi, F., Tofani, V., 2020. Using satellite interferometry to infer landslide sliding surface depth and geometry. Remote Sens. 12 (9), 1462. https://doi.org/10.3390/rs12091462.

Jaboyedoff, M., Carrea, D., Derron, M.H., Oppikofer, T., Penna, I.M., Rudaz, B., 2020. A review of methods used to estimate initial landslide failure surface depths and volumes. Eng. Geol. 267, 105478. https://doi.org/10.1016/j.enggeo.2020.105478.

Kang, Y., Lu, Z., Zhao, C.Y., Qu, W., 2023. Inferring slip-surface geometry and volume of creeping landslides based on InSAR: a case study in Jinsha River basin. Remote Sens. Environ. 294, 113620. https://doi.org/10.1016/j.rse.2023.113620.

Larsen, I.J., Montgomery, D.R., Korup, O., 2010. Landslide erosion controlled by hillslope material. Nat. Geosci. 3, 247–251. https://doi.org/10.1038/ngeo776.

Li, X., Guo, C.B., Yang, Z.H., Liao, W., Wu, R.A., Jin, J.J., He, X.Y., 2021. Development characteristics and formation mechanism of the Xiongba Giant ancient landslide in the Jinshajiang tectonic zone. Geoscience 35 (1), 47–55. https://doi.org/10.19657/j.geoscience.1000-8527.2020.095.

Li, Z.H., Zhu, W., Yu, C., Zhang, Q., Yang, Y.X., 2023. Development status and trends of imaging geodesy. Acta Geodaet. et Cartographica Sin. 52 (11), 1805–1834. https://doi.org/10.11947/j. AGCS.2023.20230003.

Liu, X.J., Zhao, C.Y., Zhang, Q., Yin, Y.P., Lu, Z., Samsonov, S., Yang, C.S., Wang, M., Tomás, R., 2021. Three-dimensional and long-term landslide displacement estimation by fusing C- and L-band SAR observations: a case study in Gongjue County, Tibet, China. Remote Sens. Environ. 267, 112745. https://doi.org/10.1016/j.rse.2021.112745.

Saroli, M., Albano, M., Atzori, S., Moro, M., Tolomei, C., Bignami, C., Stramondo, S., 2021. Analysis of a large seismically induced mass movement after the December 2018 Etna volcano (southern Italy) seismic swarm. Remote Sens. Environ. 263, 112524. https://doi.org/10.1016/j.rse.2021.112524.

Schlögel, R., Doubre, C., Malet, J.P., Masson, F., 2015. Landslide deformation monitoring with ALOS/PALSAR imagery: a D-InSAR geomorphological interpretation method. Geomorphology 231, 314–330. https://doi.org/10.1016/j.geomorph.2014.11.031.

Song, C., Yu, C., Li, Z.H., Utili, S., Frattini, P., Crosta, G., Peng, J.B., 2022. Triggering and recovery of earthquake accelerated landslides in Central Italy revealed by satellite radar observations. Nat. Commun. 13, 7278. https://doi.org/10.1038/s41467-022-35035-5.

Tihonov, A.N., 1963. Solution of incorrectly formulated problems and the regularization method. Soviet Math. Dokl. 4, 1035–1038.

Wang, B., Gao, M.L., Li, Y.M., Xu, H.H., Li, Z.H., Peng, J.B., 2023. Spatiotemporal trends of extreme temperature events along the Qinghai-Tibet plateau transportation corridor from 1981 to 2019 based on estimated near-surface air temperature. J. Geophys. Res. Atmos. 128 (22), e2023JD039040. https://doi.org/10.1029/2023JD039040.

Wegnüller, U., Werner, C., Strozzi, T., Wiesmann, A., Frey, O., Santoro, M., 2016. Sentinel-1 support in the GAMMA software. Procedia Comput. 100, 1305–1312. https://doi.org/10.1016/j.procs.2016.09.246.

Whitehouse, I.E., 1983. Distribution of large rock avalanche deposits in the central southern Alps, New Zealand. N. Z. J. Geol. Geophys. 26, 271–279. https://doi.org/10.1080/00288306.1983.10422240.

Xiao, R.Y., Yu, C., Li, Z.H., Jiang, M., He, X.F., 2022. InSAR stacking with atmospheric correction for rapid geohazard detection: applications to ground subsidence and landslides in China. Int. J. Appl. Earth Obs. Geoinf. 115, 103082. https://doi.org/10.1016/j.jag.2022.103082.

Yan, Y.Q., Guo, C.B., Zhang, Y.A., Qiu, Z.D., Li, C.H., Li, X., 2024. Development and deformation characteristics of large ancient landslides in the intensely hazardous Xiongba-Sela section of the Jinsha River, eastern Tibetan plateau. China. J Earth Sci. 35 (3), 980–997. https://doi.org/10.1007/s12583-023-1925-y.

Yao, J.M., Lan, H.X., Li, L.P., Cao, Y.M., Wu, Y.M., Zhang, Y.X., Zhou, C.D., 2022. Characteristics of a rapid landsliding area along Jinsha River revealed by multi-temporal remote sensing and its risks to Sichuan-Tibet railway. Landslides 19, 703–718. https://doi.org/10.1007/s10346-021-01790-7.

Yu, C., Li, Z.H., Penna, N.T., Crippa, P., 2018. Generic atmospheric correction model for interferometric synthetic aperture radar observations. J. Geophys. Res. Solid Earth 123, 9202–9222. https://doi.org/10.1029/2017JB015305.

Yu, C., Li, Z.H., Penna, N.T., 2020. Triggered afterslip on the southern Hikurangi subduction interface following the 2016 Kaikura earthquake from InSAR time series with atmospheric corrections. Remote Sens. Environ. 251, 112097. https://doi.org/10.1016/j.rse.2020.112097.

Zhang, X., Liu, L.Y., Chen, X.D., Gao, Y., Xie, S., Mi, J., 2021. GLC_FCS30: global land-cover product with fine classification system at 30 m using time-series Landsat imagery. Earth Syst. Sci. Data 13, 2753–2776. https://doi.org/10.5194/essd-13-2753-2021.

Zhang, C.L., Li, Z.H., Yu, C., Chen, B., Ding, M.T., Zhu, W., Yang, J., Liu, Z.J., Peng, J.B., 2022. An integrated framework for wide-area active landslide detection with InSAR observations and SAR pixel offsets. Landslides 19 (12), 2905–2923. https://doi.org/10.1007/s10346-022-01954-z.

Zhu, S.N., Yin, Y.P., Wang, M., Zhu, M., Wang, C.H., Wang, W.P., Li, J.F., Zhao, H., 2021. Instability mechanism and disaster mitigation measures of long-distance landslides at high location in Jinsha River junction zone: case study of Sela landslide in Jinsha River. Tibet. Chin. J. Geotech. 43 (4), 688–697 (In Chinese). 10.11779/CJGE202104011.

Zhu, W., Yang, L.Y., Cheng, Y.Q., Liu, X.Y., Zhang, R.X., 2024. Active thickness estimation and failure simulation of translational landslide using multi-orbit InSAR observations: a case study of the Xiongba landslide. Int. J. Appl. Earth Obs. Geoinf. 119, 103801. https://doi.org/10.1016/j.jag.2024.103801.